Ann. Geophys., 29, 551–562, 2011
www.ann-geophys.net/29/551/2011/
doi:10.5194/angeo-29-551-2011

Annales Geophysicae

Feasibility study on Generalized-Aurora Computed Tomography

Y.-M. Tanaka[1], T. Aso[2], B. Gustavsson[3], K. Tanabe[4], Y. Ogawa[1], A. Kadokura[1], H. Miyaoka[1], T. Sergienko[5], U. Brändström[5], and I. Sandahl[5]

[1]National Institute of Polar Research, Tokyo, Japan
[2]The Graduate University for Advanced Studies (Sokendai), Japan
[3]Department of Communication Systems, Lancaster University, UK
[4]Faculty of Science and Engineering, Waseda University, Tokyo, Japan
[5]Swedish Institute of Space Physics, Kiruna, Sweden

Received: 6 September 2010 – Revised: 14 February 2011 – Accepted: 16 February 2011 – Published: 15 March 2011

Abstract. Aurora Computed Tomography (ACT) is a method for retrieving the three-dimensional (3-D) distribution of the volume emission rate from monochromatic auroral images obtained simultaneously by a multi-point camera network. We extend this method to a Generalized-Aurora Computed Tomography (G-ACT) that reconstructs the energy and spatial distributions of precipitating electrons from multi-instrument data, such as ionospheric electron density from incoherent scatter radar, cosmic noise absorption (CNA) from imaging riometers, as well as the auroral images. The purpose of this paper is to describe the reconstruction algorithm involved in this method and to test its feasibility by numerical simulation. Based on a Bayesian model with prior information as the smoothness of the electron energy spectra, the inverse problem is formulated as a maximization of posterior probability. The relative weighting of each instrument data is determined by the cross-validation method. We apply this method to the simulated data from real instruments, the Auroral Large Imaging System (ALIS), the European Incoherent Scatter (EISCAT) radar at Tromsø, and the Imaging Riometer for Ionospheric Study (IRIS) at Kilpisjärvi. The results indicate that the differential flux of the precipitating electrons is well reconstructed from the ALIS images for the low-noise cases. Furthermore, we demonstrate in a case study that the ionospheric electron density from the EISCAT radar is useful for improving the reconstructed electron flux. On the other hand, the incorporation of CNA data into this method is difficult at this stage, because the extension of energy range to higher energy causes a difficulty in the reconstruction of the low-energy electron flux. Nevertheless, we expect that this method may be useful in analyzing multi-instrument data and, in particular, 3-D data, which will be obtained in the upcoming EISCAT_3D.

Keywords. Magnetospheric physics (Auroral phenomena)

Correspondence to: Y.-M. Tanaka
(ytanaka@nipr.ac.jp)

1 Introduction

In the past, techniques for analyzing auroral data have dealt primarily with a single type of observational data in one or two dimensions. In recent year, however, many different kinds of auroral data have been obtained by comprehensive observations using a variety of instruments. Furthermore, new projects involving three-dimensional (3-D) ionospheric observations such as EISCAT_3D are planned in the near future. Detailed information of the EISCAT_3D project is described in the web page http://www.eiscat3d.se. Thus, new analysis methods are required that can evaluate data from multiple instruments in addition to 3-D data.

One promising methods is Aurora Computed Tomography (ACT), which reconstructs the 3-D distribution of auroral luminosity from monochromatic images obtained simultaneously at multi-point stations (e.g., Aso et al., 1990, 1993, 1998; Frey and Frey, 1996; Nygrén et al., 1996). In previous studies, the determination of the altitude of auroral emissions was performed by using a meridian scanning photometer chain or stereo TV cameras (Romick and Belon, 1967; Stenbaek-Nielsen and Halliman, 1979; Vallance Jones et al., 1991; Dashkevich et al., 2007). The tomographic inversion technique for aurora analysis has been developed with the construction of ground-based camera networks such as the Auroral Large Imaging System (ALIS) (Gustavsson, 1998; Brändström, 2003). In particular, algebraic reconstruction techniques (ARTs) such as MART (Muliplicative Algebraic Reconstruction Technique) and SIRT (Simultaneous Iterative

Published by Copernicus Publications on behalf of the European Geosciences Union.

Reconstruction Technique) were often adopted for the reconstruction algorithm (Gordon et al., 1970; Tanabe 1971). Auroral tomography is generally an under-determined and ill-posed problem due to the limited number of ground-based stations. Therefore, prior information on the auroral luminosity was used to regularize the inverse problem.

The altitude profile of auroras obtained by tomographic inversion provides us with important information about the energy spectra of precipitating electrons, the mechanism of auroral emission, and the atmospheric gas. Gustavsson et al. (2001) estimated the energy distribution of incident electrons from the volume emission rate of the 427.8-nm emission based on the inversion technique. Janhunen (2001) presented an excellent technique for retrieving the precipitating electron flux directly from multi-wavelength all-sky images without reconstruction of the 3-D volume emission rate as an intermediate step.

In northern Scandinavia, there are a number of instruments other than ALIS, such as the European Incoherent Scatter (EISCAT) radar and the Imaging Riometer for Ionospheric Study (IRIS) at Kilpisjärvi (Folkestad et al., 1983; Detrick and Rosenberg, 1990). Similar to auroral emission, both the electron density obtained from the EISCAT radar and the cosmic noise absorption (CNA) from the imaging riometer are closely related to the precipitating electron flux. Thus, it is possible for us to combine all these data to allow reconstruction of the precipitating electron flux. Aso et al. (2008) have proposed a concept of a generalized tomographic inversion technique to reconstruct the differential flux of auroral precipitating electrons from multi-instrument data using a Bayesian model. We call this method as a Generalized-Aurora Computed Tomography (G-ACT).

The G-ACT method is capable of retrieving the horizontal 2-D map of the primary auroral electron precipitation. Thus, this method is suitable for researches on the temporal and spatial development of the precipitating electron flux for various types of auroras, such as the quiet arc during the substorm growth phase, multiple auroral arcs, folds and spirals. In particular, the coordinated observations with the EISCAT_3D will allow us to estimate the precipitating electron flux more accurately. The comparison of the precipitating electron flux with the neutral and plasma parameters will be useful in investigating the influence of the auroral precipitation on the neutral atmosphere and the magnetosphere-ionosphere coupling process of small scale auroral phenomena, including the 3-D current system in the nonuniform ionosphere and the active role of the ionosphere.

In this paper, we present the concrete algorithm of the G-ACT in detail, based on Aso et al. (2008), and test the feasibility of this method by numerical simulation. We apply this method to some specific cases, in which we assume a simple but realistic electron energy distribution, station location, and observational noise. In general, the reconstruction results depend on several factors including the auroral form, the geometric constellation between the aurora and the observation stations, the number of instruments, and noise in the observational data. The reconstruction tests under various more complicated conditions will be explored in future work.

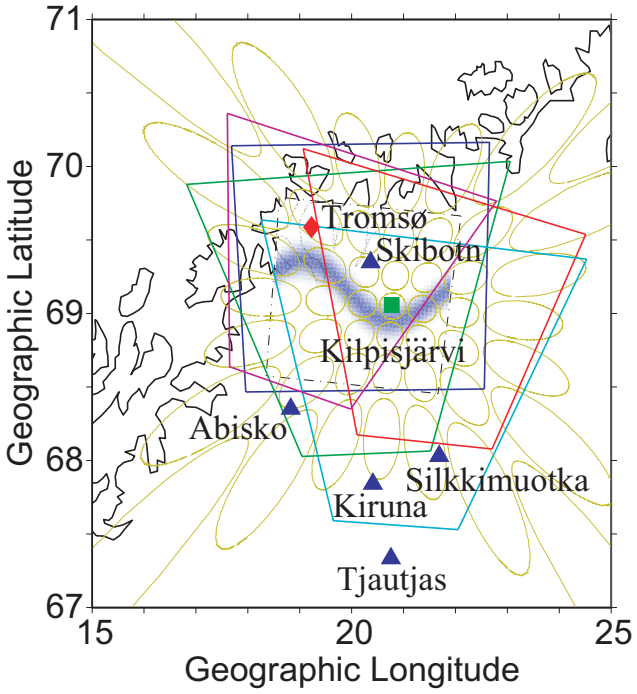

Fig. 1. Location of stations used in this paper. The quadrangles correspond to the fields of view of the ALIS imagers mapped to 110 km altitude and the ovals show −3 dB contour of the main beams of the IRIS at 90 km. The square surrounded by a dashed line indicates the simulation region at 110 km alitutde. Note that this figure shows one example of the fields of view for each instrument and is valid only for the calculation in this paper.

2 Forward problem

2.1 Instrumentation

Figure 1 shows the location of the stations used in this study, and their coordinates are listed in Table 1. In Fig. 1, the fields of view of the ALIS imagers at 110 km altitude and the −3 dB contour of the main beams of the IRIS at 90 km are also shown together with the simulation region. It was assumed that aurora was observed simultaneously by five imagers comprising ALIS, the EISCAT radar at Tromsø, and the IRIS at Kilpisjärvi.

ALIS consists of unmanned remote-controlled CCD imagers with 1024×1024 pixels resolution and it is assumed that the pixels are binned to 256×256. The observation mode of ALIS is assumed to be the EISCAT mode, in which all cameras are directed to the ionospheric region over the EISCAT Tromsø site. The field of view of each camera is

Table 1. Coordinates of stations used in this paper.

No.	Station Name	Latitude	Longitude	Altitude	Instrument Type
1	Skibotn	69°21′00.0″	20°21′36.0″	200 m	ALIS
2	Kiruna	67°50′26.6″	20°24′40.0″	425 m	ALIS
3	Silkkimuotka	68°01′47.0″	21°41′13.4″	385 m	ALIS
4	Tjautjas	67°20′02.4″	20°45′23.2″	470 m	ALIS
5	Abisko	68°21′06.5″	18°49′35.0″	360 m	ALIS
6	Tromsø	69°35′11″	19°13′38″	86 m	EISCAT radar
7	Kilpisjärvi	69.050°	20.790°	0 m	IRIS

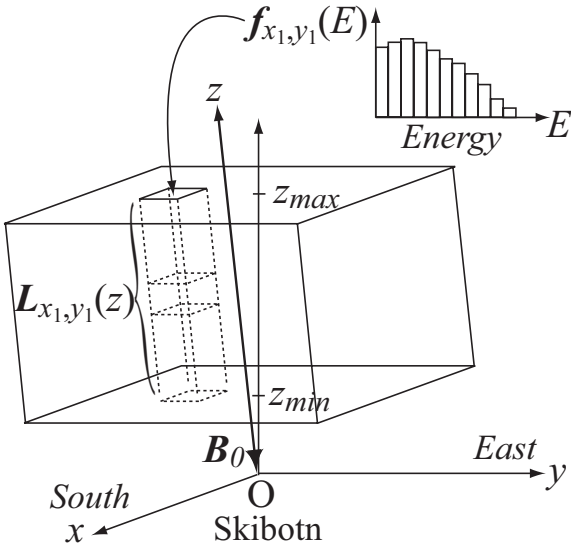

Fig. 2. Coordinate system used in this study. $\boldsymbol{B}_0$ is the directional vector of the geomagnetic field.

between about 60 to 90°, which corresponds to about 0.6 to 1.2 km spatial resolution at an altitude of 100 km over Tromsø. The monochromatic filter and exposure time of the ALIS imager can be programmably changed during the observation. Of the observed wavelengths (427.8, 557.7, 630.0, 844.6 nm, etc.), it is assumed that the wavelength of 427.8 nm is used for all the stations, because this wavelength corresponds to a simple emission process. The details of ALIS are described in Brändström (2003).

The EISCAT UHF radar is assumed to be operating in CP1 mode, which measures plasma parameters along the geomagnetic field line direction from Tromsø (Elevation angle of 77.4 degrees and azimuth angle of 185.8 degrees). It is also assumed that the electron density is detected at altitudes between 102 and 166 km at intervals of 4 km. To reduce the observational error, the radar observation generally requires the integration of data over several minutes. Thus, it is taken as implicit that the aurora is stable during the integration period.

The IRIS system installed at Kilpisjärvi, Finland, has an 8×8-element dipole antenna array and produces 49 independent beams in an area of about $200 \times 200\,\mathrm{km}^2$ at an altitude of 90 km. It produces a 2-D image of CNA at a frequency of 38.2 MHz every second. CNA is generally due to electron density enhancement in the ionospheric D region, which is primarily caused by precipitating electrons with energies above 20×10^3 eV. Hence, it is expected that CNA may contribute to improving the reconstruction of the electron flux in the high-energy range.

2.2 Calculation of auroral emission and electron density enhancement in the ionosphere

Figure 2 shows the coordinate system used for both forward and inverse analyses. We adopted an oblique coordinate system with the origin (O) at Skibotn, the x-axis anti-parallel to the horizontal component of the geomagnetic field, the y-axis eastward, and the z-axis anti-parallel to the geomagnetic field. Here, the z-coordinate does not signify distance from O but rather altitude. The simulation region was $-50 \sim 88$ km, $-73 \sim 65$ km, and $80 \sim 230$ km for the x-, y-, and z-directions, respectively, and an energy (E) range of $300 \sim 20 \times 10^3$ eV or $300 \sim 100 \times 10^3$ eV was used. This region was divided linearly into $n_x \times n_y \times n_z$ voxels along the x-, y-, and z-axes and logarithmically into n_E in the E direction. We set the parameters (n_x, n_y, n_z, n_E) to (46, 46, 50, 50), corresponding to a spatial mesh size of $3 \times 3 \times 3\,\mathrm{km}^3$. These parameters were selected so that all voxels have at least one crossing of the line of sight of the pixels in the auroral images.

The incident electrons at a location (x_1, y_1, $z_{\max}$(=230 km)) cause auroral emission in the voxels below $z_{\max}$ along a field line. We define a vector $\boldsymbol{f}_{x_1,y_1}(E) = \{f_i | i = 1,2,....,n_E\}$ [$\mathrm{m}^{-2}\,\mathrm{s}^{-1}\,\mathrm{eV}^{-1}$] for the differential flux of the incident electrons at (x_1, y_1, $z_{\max}$) and $\boldsymbol{L}_{x_1,y_1}(z) = \{L_i | i = 1,2,....,n_z\}$ [$\mathrm{m}^{-3}\,\mathrm{s}^{-1}$] for the 427.8-nm volume emission rate at (x_1, y_1, z), where f_i is the differential flux in energy between E_i and $E_i + \Delta E_i$ and L_i is the volume emission rate at the altitude between z_i and

$z_i + \Delta z_i$. The relation between $\boldsymbol{f}_{x_1,y_1}(E)$ and $\boldsymbol{L}_{x_1,y_1}(z)$ is given by

$$\boldsymbol{L}_{x_1,y_1} = \mathbf{m}_1 \boldsymbol{f}_{x_1,y_1}, \tag{1}$$

where $\mathbf{m}_1$ is a $n_z \times n_E$ matrix for calculating $\boldsymbol{L}_{x_1,y_1}(z)$ from $\boldsymbol{f}_{x_1,y_1}(E)$ and is described in detail in the Appendix. Assuming that $\mathbf{m}_1$ is independent of x_1 and y_1, Eq. (1) can be expanded in the x- and y-directions as follows:

$$\begin{pmatrix} \boldsymbol{L}_{1,1} \\ \boldsymbol{L}_{1,2} \\ \vdots \\ \boldsymbol{L}_{n_x,n_y} \end{pmatrix} = \begin{pmatrix} \mathbf{m}_1 & 0 & \cdots & 0 \\ 0 & \mathbf{m}_1 & \ddots & \vdots \\ \vdots & \ddots & \ddots & 0 \\ 0 & \dots & 0 & \mathbf{m}_1 \end{pmatrix} \begin{pmatrix} \boldsymbol{f}_{1,1} \\ \boldsymbol{f}_{1,2} \\ \vdots \\ \boldsymbol{f}_{n_x,n_y} \end{pmatrix}, \tag{2}$$

$$\boldsymbol{L} = \mathbf{M}_1 \boldsymbol{f}. \tag{3}$$

In Eq. (3), $\boldsymbol{f}$ and $\boldsymbol{L}$ are functions of x and y as well as E and z, i.e., $\boldsymbol{f}(x,y,E) = \{f_i | i = 1,2,....,n\}$ and $\boldsymbol{L}(x,y,z) = \{L_i | i = 1,2,....,m\}$, where $n = n_E \times n_x \times n_y$ and $m = n_z \times n_x \times n_y$. $\mathbf{M}_1$ is a large sparse matrix defined by

$$\mathbf{M}_1 = \begin{pmatrix} \mathbf{m}_1 & 0 & \cdots & 0 \\ 0 & \mathbf{m}_1 & \ddots & \vdots \\ \vdots & \ddots & \ddots & 0 \\ 0 & \dots & 0 & \mathbf{m}_1 \end{pmatrix}. \tag{4}$$

In a similar manner to $\boldsymbol{L}$, we define $\boldsymbol{D}(x,y,z) = \{D_i | i = 1,2,....,m\}$ [m^{-6}] as a square of ionospheric electron density generated by the incident electrons. $\boldsymbol{D}$ has a linear relationship with respect to $\boldsymbol{f}$, as shown by

$$\boldsymbol{D} = \mathbf{M}_2 \boldsymbol{f}, \tag{5}$$

where

$$\mathbf{M}_2 = \begin{pmatrix} \mathbf{m}_2 & 0 & \cdots & 0 \\ 0 & \mathbf{m}_2 & \ddots & \vdots \\ \vdots & \ddots & \ddots & 0 \\ 0 & \dots & 0 & \mathbf{m}_2 \end{pmatrix}. \tag{6}$$

Again, $\mathbf{m}_2$ is a $n_z \times n_E$ matrix for obtaining $\boldsymbol{D}_{x_1,y_1}(z)$ from $\boldsymbol{f}_{x_1,y_1}(E)$ (see Appendix).

2.3 Projection to observational data

In this subsection, we formulate the projection of the volume emission rate $\boldsymbol{L}(x,y,z)$ and the square of ionospheric electron density $\boldsymbol{D}(x,y,z)$ to the observational data, i.e., auroral images from the ALIS, electron density from the EISCAT radar, and CNA from the IRIS at Kilpisjärvi.

A gray level g_i [photons m^{-2} s^{-1} ster^{-1}] at a pixel i in the auroral image is approximated by a linear integration along a line of sight, as follows:

$$g_i = \frac{c_g(\theta,\phi)}{4\pi} \int L(r,\theta,\phi) dr, \tag{7}$$

where (r,θ,ϕ) are polar coordinates whose origin is located at the center of the camera lens, and $c_g(\theta,\phi)$ is a sensitivity and vignetting factor (Aso et al., 1990). Atmospheric attenuation was ignored in this study. Equation (7) is expressed by the matrix operation

$$\boldsymbol{g} = \mathbf{P}_1 \boldsymbol{L} = \mathbf{P}_1 \mathbf{M}_1 \boldsymbol{f}, \tag{8}$$

where $\boldsymbol{g} = \{g_i | i = 1,2,....,l_g\}$ is a gray-level vector whose length is l_g and $\mathbf{P}_1$ is a $l_g \times m$ matrix used to calculate $\boldsymbol{g}$ by integrating $\boldsymbol{L}$ in Eq. (3) along the line of sight, and includes the sensitivity and vignetting factor.

For the EISCAT radar, the location of the observation points in the ionosphere is known. The square of electron density at the observation points of the EISCAT radar, $\mathbf{d} = \{d_i | i = 1,2,....,l_d\}$ [m^{-6}], can be given by the matrix expression

$$\mathbf{d} = \mathbf{P}_2 \boldsymbol{D} = \mathbf{P}_2 \mathbf{M}_2 \boldsymbol{f}, \tag{9}$$

where $\mathbf{P}_2$ is a $l_d \times m$ matrix that derives data at the voxels including the radar observation points from $\boldsymbol{D}(x,y,z)$ in Eq. (5).

CNA a_i [dB] measured at beam i of the IRIS is approximated by

$$a_i = \frac{c_a}{\omega^2} \int \sqrt{D(r,\theta,\phi)}\, \nu(r,\theta,\phi) dr, \tag{10}$$

where (r,θ,ϕ) are polar coordinates whose origin is at Kilpisjärvi, ω is the observation angular frequency ($\omega = 2\pi \times 38.2$ [MHz]), ν is the electron-neutral collision frequency, and c_a is a constant with a value of 4.6×10^{-5} in MKS units. It should be noted that in Eq. (10) we assumed that the main lobe is very sharp and the effect of side lobes is small, although this assumption is not always practical, particularly for the beams on the edge (Hargreaves and Detrick, 2002). Then, the vector $\boldsymbol{a} = \{a_i | i = 1,2,....,l_a\}$ is given by

$$\boldsymbol{a} = \mathbf{P}_3 \sqrt{\boldsymbol{D}} = \mathbf{P}_3 \sqrt{\mathbf{M}_2 \boldsymbol{f}}, \tag{11}$$

where $\mathbf{P}_3$ is a $l_a \times m$ matrix operator that integrates the product of $\sqrt{D}$ and ν along the line of sight. We note that the square root in Eq. (11) applies to all elements of the vector. ν was derived from Table 3a of Aggarwal et al. (1979) and it was assumed to be dependent only on the altitude z.

Finally, we added noise to $\boldsymbol{g}$, $\boldsymbol{d}$, and $\boldsymbol{a}$ to obtain the observational data, $\tilde{\boldsymbol{g}}$, $\tilde{\boldsymbol{d}}$, and $\tilde{\boldsymbol{a}}$ (in this paper a tilde "$\sim$" signifies observational data).

3 Inverse problem

3.1 Bayesian model

The inverse problem is based on the Bayesian model and is formulated as a problem of maximization of posterior probability. We define $P(\tilde{\boldsymbol{b}}|\boldsymbol{f})$ as the probability of observing data

$\tilde{\boldsymbol{b}}$ given model $\boldsymbol{f}$, and $P(\boldsymbol{f})$ as the prior probability of model $\boldsymbol{f}$. According to Bayes' theorem, the posterior probability $P(\boldsymbol{f}|\tilde{\boldsymbol{b}})$, which is the probability that model $\boldsymbol{f}$ is true given observational data $\tilde{\boldsymbol{b}}$, is expressed by

$$P(\boldsymbol{f}|\tilde{\boldsymbol{b}}) = \frac{P(\tilde{\boldsymbol{b}}|\boldsymbol{f})P(\boldsymbol{f})}{P(\tilde{\boldsymbol{b}})} \propto P(\tilde{\boldsymbol{b}}|\boldsymbol{f})P(\boldsymbol{f}), \tag{12}$$

where $P(\tilde{\boldsymbol{b}})$ is the marginal probability of $\tilde{\boldsymbol{b}}$. $\tilde{\boldsymbol{b}}$ corresponds to the observational data $\tilde{\boldsymbol{g}}$, $\tilde{\boldsymbol{d}}$, and $\tilde{\boldsymbol{a}}$ in Sect. 2.

We adopted a smoothness constraint of $\boldsymbol{f}$ for the prior probability of $\boldsymbol{f}$, as given by

$$P(\boldsymbol{f}) \propto \exp\left(-\frac{\left\|\nabla^2 \boldsymbol{f}\right\|^2}{2\sigma^2}\right), \tag{13}$$

where σ^2 is the variance of $\nabla^2 \boldsymbol{f}$ and the second-order derivative of $\boldsymbol{f}$ is taken with respect to x, y, and E. Assuming that data $\tilde{\boldsymbol{b}}$ has Gaussian errors, the likelihood is expressed by

$$P(\tilde{\boldsymbol{b}}|\boldsymbol{f}) \propto \exp\left\{-\sum_j \frac{1}{2}\left(\tilde{\boldsymbol{b}}_j - \boldsymbol{b}_j(\boldsymbol{f})\right)^T \boldsymbol{\Sigma}_j^{-1}\left(\tilde{\boldsymbol{b}}_j - \boldsymbol{b}_j(\boldsymbol{f})\right)\right\}, \tag{14}$$

where j signifies the kind of data. $\tilde{\boldsymbol{b}}_j$ corresponds to $\tilde{\boldsymbol{g}}$, $\tilde{\boldsymbol{d}}$, and $\tilde{\boldsymbol{a}}$ for $j = 1$, 2, and 3, respectively, and $\boldsymbol{b}_j(\boldsymbol{f})$ corresponds to $\boldsymbol{g}$, $\boldsymbol{d}$, and $\boldsymbol{a}$. $\boldsymbol{\Sigma}_j^{-1}$ is the inverse covariance matrix. Assuming that the data are independent from each other, $\boldsymbol{\Sigma}_j^{-1}$ has zero off-diagonal elements and the inverse variances in the diagonal elements.

The properties of the inverse covariance matrix $\boldsymbol{\Sigma}_j^{-1}$ for each kind of data are described below. Since the photon count detected by the ALIS CCD follows Poisson statistics, the standard deviation of the noise equals the square root of the mean. When the mean value of the photon count is large enough, the Poisson distribution can be approximated by a Gaussian distribution. Thus, we assumed that the (i, i)-th entry of $\boldsymbol{\Sigma}_1^{-1}$ is $1/\tilde{g}_i$. For the electron density and CNA, on the other hand, it was assumed that the noise was the same for all data elements. This assumption allows us to change $\boldsymbol{\Sigma}_2^{-1}$ and $\boldsymbol{\Sigma}_3^{-1}$ to $1/\sigma_2^2 \cdot \mathbf{I}$ and $1/\sigma_3^2 \cdot \mathbf{I}$, respectively, where σ_2^2 and σ_3^2 are the variances of the electron density and CNA and $\mathbf{I}$ is an identity matrix.

By substituting Eqs. (13) and (14) into (12), $P(\boldsymbol{f}|\tilde{\boldsymbol{b}})$ is given by

$$P(\boldsymbol{f}|\tilde{\boldsymbol{b}}) \propto \exp\left[-\frac{1}{2\sigma^2}\left\{\sum_j w_j^2\left(\tilde{\boldsymbol{b}}_j - \boldsymbol{b}_j(\boldsymbol{f})\right)^T \boldsymbol{\Sigma}_j^{-1}\left(\tilde{\boldsymbol{b}}_j - \boldsymbol{b}_j(\boldsymbol{f})\right) + \left\|\nabla^2 \boldsymbol{f}\right\|^2\right\}\right], \tag{15}$$

where w_j^2 are σ^2, σ^2/σ_2^2, and σ^2/σ_3^2 for $j = 1$, 2, and 3, respectively, and $\boldsymbol{\Sigma}_2^{-1}$ and $\boldsymbol{\Sigma}_3^{-1}$ can be replaced with the identity matrices. w_j are the so-called hyper-parameters, which are constants corresponding to the weighting factor for each instrument data. To maximize the posterior probability, it is necessary to minimize the function:

$$\varphi(\boldsymbol{f}; w_j) = \sum_j w_j^2\left(\tilde{\boldsymbol{b}}_j - \boldsymbol{b}_j(\boldsymbol{f})\right)^T \boldsymbol{\Sigma}_j^{-1}\left(\tilde{\boldsymbol{b}}_j - \boldsymbol{b}_j(\boldsymbol{f})\right) + \left\|\nabla^2 \boldsymbol{f}\right\|^2 = \left\|\boldsymbol{r}(\boldsymbol{f}; w_j)\right\|^2, \tag{16}$$

where

$$\boldsymbol{r}(\boldsymbol{f}; w_j) = \begin{pmatrix} w_1 \boldsymbol{\Sigma}_1^{-\frac{1}{2}}\left(\tilde{\boldsymbol{g}} - \boldsymbol{g}(\boldsymbol{f})\right) \\ w_2\left(\tilde{\boldsymbol{d}} - \boldsymbol{d}(\boldsymbol{f})\right) \\ w_3\left(\tilde{\boldsymbol{a}} - \boldsymbol{a}(\boldsymbol{f})\right) \\ \nabla^2 \boldsymbol{f} \end{pmatrix}. \tag{17}$$

It should be noted that $\min[\varphi(\boldsymbol{f}; w_j)]$ is a non-linear least squares problem with respect to $\boldsymbol{f}$, because Eq. (16) includes the square root of $\boldsymbol{f}$ for CNA data (see Eq. 11).

3.2 Ad hoc modification of f by non-negative constraint and method to solve the minimization problem

To take advantage of the non-negative constraint of the differential flux $\boldsymbol{f}$ (i.e., $\boldsymbol{f} \geq 0$), the change of variables, $\boldsymbol{f} = \exp(\boldsymbol{x})$, was carried out. Then, $\min[\varphi(\boldsymbol{x}; w_j)]$ is a non-linear least squares problem with respect to $\boldsymbol{x}$, even if CNA is not used for data analysis. We solved this problem by the Gauss-Newton algorithm.

In the Gauss-Newton method, the parameter $\boldsymbol{x}$ proceeds by the iteration, $\boldsymbol{x}^{(k+1)} = \boldsymbol{x}^{(k)} + \Delta\boldsymbol{x}^{(k)}$, where the increment $\Delta\boldsymbol{x}^{(k)}$ at the k-th step is a solution of the following equation:

$$\left(\mathbf{J}^T(\boldsymbol{x}^{(k)})\mathbf{J}(\boldsymbol{x}^{(k)})\right)\Delta\boldsymbol{x}^{(k)} = -\mathbf{J}^T(\boldsymbol{x}^{(k)})\boldsymbol{r}(\boldsymbol{x}^{(k)}). \tag{18}$$

Here, $\mathbf{J}(\boldsymbol{x})$ is the Jacobian matrix of $\boldsymbol{r}(\boldsymbol{x})$ with respect to $\boldsymbol{x}$. $\mathbf{J}(\boldsymbol{x})$ can easily be obtained, if the derivative of $\boldsymbol{r}(\boldsymbol{x})$ with respect to $\boldsymbol{x}$ can be analytically solved such as in this case. Equation (18) is a normal equation with a large sparse matrix; therefore, we solved it by the Conjugate Gradient (CG) method.

The Gauss-Newton method requires an initial guess $\boldsymbol{x}^{(0)}$. Since it is not sure that the posterior distribution has only a single maximum and that this method can always find the highest one, we need to select a suitable initial value for $\boldsymbol{x}^{(0)}$ carefully. Thus, we first used only gray level $\tilde{\boldsymbol{g}}$ to solve $\min[\varphi(\boldsymbol{f})]$ with respect to $\boldsymbol{f}$, which yielded a linear least squares problem. We solved the problem by the SIRT method with $\boldsymbol{f}^{(0)} = 10^7$ [$\mathrm{m^{-2}\,s^{-1}\,eV^{-1}}$] and used the solution $\boldsymbol{f}^*$ for the initial value of the Gauss-Newton algorithm (i.e., $\boldsymbol{x}^{(0)} = \log(\boldsymbol{f}^*)$).

3.3 Determination of hyper-parameters (w_1, w_2, w_3)

Unfortunately, there is no information of the hyper-parameters. We used the 10-fold cross-validation method to determine the hyper-parameters (Stone, 1974). First, the full

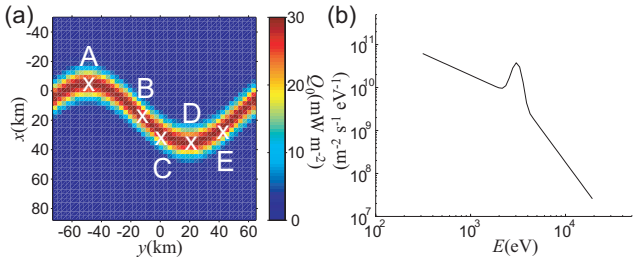

Fig. 3. **(a)** Spatial distribution of total energy flux (Q_0) of incident electrons at 230-km altitude. Top and right correspond to the northward and eastward direction, respectively. The cross marked A indicated the line-of-sight direction of the EISCAT radar. **(b)** Energy distribution of incident electrons at point A. The distribution was produced in almost the same way as Strickland et al. (1993).

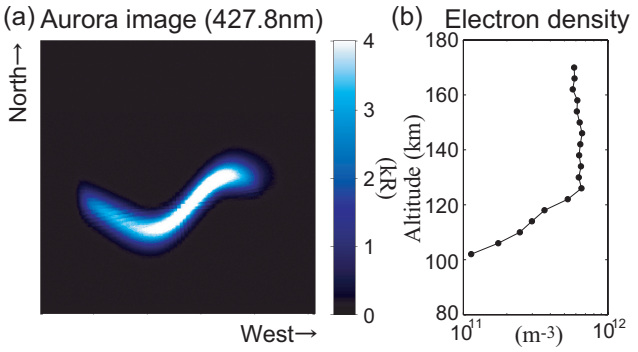

Fig. 4. **(a)** Auroral image at a wavelength of 427.8 nm observed with CCD imager at Skibotn. Gray levels in this image include a background noise of 300 R. **(b)** Electron density measured with the EISCAT radar at Tromsø. The electron density includes a Gaussian noise with a mean of 0 m^{-3} and a standard deviation of 3% of the density.

data set was divided into 10 subsets, where the k-th subset consists of the k-th, $(k+10)$-th, $(k+20)$-th, ... elements of the vectors $\tilde{\boldsymbol{g}}$, $\tilde{\boldsymbol{d}}$, and $\tilde{\boldsymbol{a}}$. Then, the cross validation score for the assumed hyper-parameters (w_1, w_2, w_3) was calculated as follows.

Of the 10 subsets, one was selected as a test set ($\tilde{\boldsymbol{b}}_j^{\mathrm{tes}}$) and the others as a training set ($\tilde{\boldsymbol{b}}_j^{\mathrm{tra}}$). We found the solution $\hat{\boldsymbol{x}}$ to minimize $\varphi(\boldsymbol{x}; w_1, w_2, w_3)$ using only the training set $\tilde{\boldsymbol{b}}_j^{\mathrm{tra}}$ and then the test set was predicted from $\boldsymbol{b}_j^{\mathrm{tes}}(\hat{\boldsymbol{x}})$. We then calculated the sum of the squares of the residuals between the test data and the predicted data:

$$\delta(w_1, w_2, w_3) = \sum_j \left\| \tilde{\boldsymbol{b}}_j^{\mathrm{tes}} - \boldsymbol{b}_j^{\mathrm{tes}}(\hat{\boldsymbol{x}}) \right\|^2. \quad (19)$$

The cross-validation score $\bar{\delta}(w_1, w_2, w_3)$ was calculated by averaging over 10 $\delta(w_1, w_2, w_3)$s, which were obtained by replacing the test set with one of the training sets in turn.

The values of w_1, w_2, and w_3 required to minimize $\bar{\delta}(w_1, w_2, w_3)$ was determined by a trial and error method. In addition to the hyper-parameters, the number of iterations for the Gauss-Newton algorithm was also simultaneously determined so as to minimize $\bar{\delta}$.

Furthermore, we set the upper limit of the hyper-parameters. The reconstructed results were poor without the upper limit for several cases, in which the smoothness of energy and spatial distributions of differential flux was much weaker than expected. The reconstructed results using the hyper-parameters determined by the cross-validation method tend to fit the observational data more closely than the prior distribution (i.e., smoothness constraint). The upper limits of the hyper-parameters were determined by a trial and error method so as to suppress the reconstruction error but retrieve the substantial spectral peak to some extent. The upper limit values were fixed through this paper.

4 Results and discussions

4.1 Reconstruction from multiple auroral images

In this subsection, we demonstrate a reconstruction using only multiple auroral images. Figure 3 shows the spatial and energy distributions of the incident electrons assumed for the forward problem. The auroral arc was assumed to have a sinusoidal shape in the y-direction and a Gaussian shape in the x-direction. The total energy flux (Q_0) of the incident electrons has a maximum value of 30 m Wm^{-2} at the center of the arc. The energy distribution was assumed to be Gaussian with low- and the high-energy slopes, which has been reported by Strickland et al. (1993) to be typical of auroral electrons. The position of the energy peak (E_P) varies linearly from 2×10^3 to 8×10^3 eV with increasing longitude. The scaling exponents of the power-law distributions were set to -1.0 and -3.0 for low-energy and high-energy slopes, respectively, and the values of these distributions at $E = E_P$ were assumed to be equal to 0.2 times of the peak value of the Gaussian distribution. The pitch angle distribution was assumed to be isotropic.

Figure 4 shows the 427.8-nm auroral image observed at Skibotn and the electron density profile measured with the EISCAT radar at Tromsø. The gray levels in Fig. 4 include a background noise (N_B) of 300 R. Since the gray level noise for a pixel i was assumed to have the standard deviation of $\sqrt{g_i + N_B}$, the standard deviation is greater than $\sqrt{300}$ R for all pixels. The electron density includes a Gaussian noise with a mean of 0 m^{-3} and a standard deviation of 3% of the density.

Figure 5 shows the reconstructed Q_0 from five auroral images for various amount of noise levels. The reconstruction is accurate for the case of low noise (see Fig. 5a and b). As the noise increases, however, some regions suffer from

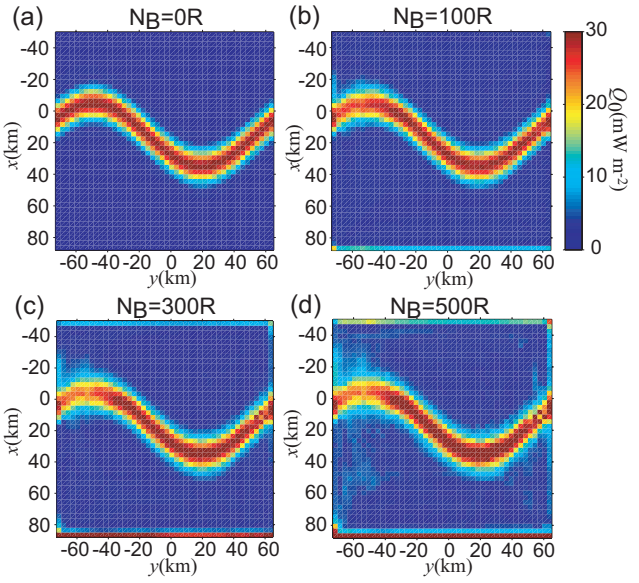

Fig. 5. The dependence of reconstructed total energy flux (Q_0) on noise. Background noise of **(a)** 0 R, **(b)** 100 R, **(c)** 300 R, and **(d)** 500 R has been added to the auroral images for all five ALIS stations.

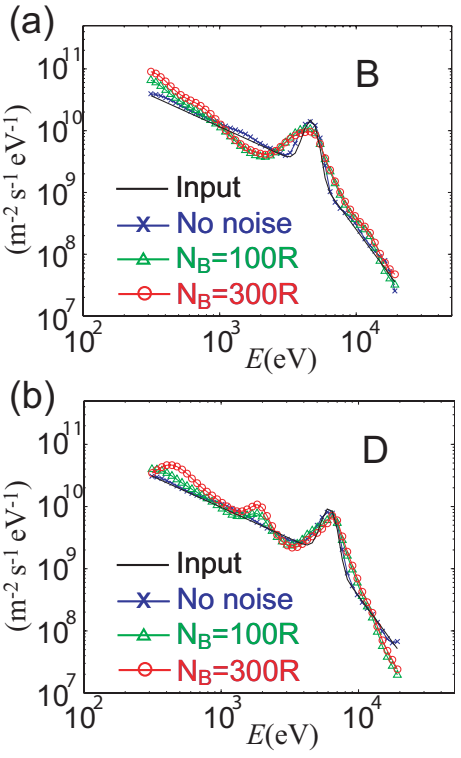

Fig. 6. Differential flux of the incident electrons reconstructed from only auroral images. **(a)** and **(b)** show the results for points B and D in Fig. 3a, respectively. Black and blue curves represent the differential flux of the original incident electrons and the differential flux reconstructed from auroral images with no noise, respectively. Green and red curves correspond to the differential flux reconstructed from images with a background noise of 100 and 300 R, respectively.

underestimation or overestimation of the energy flux. One example is the northern and southern boundaries of the reconstruction region where Q_0 is highly overestimated, and another is the western part of the arc at $y = -73 \sim -40$ km where Q_0 is slightly underestimated (see Fig. 5c and d). The latter is attributed to the position of the ALIS stations, because four of five stations lie to the south of the reconstruction region (see Fig. 1). We have already confirmed that the underestimation of Q_0 in the arc at $y = -73 \sim -40$ km is improved by moving one of four southern stations (ex., Tjautjas) to the north of auroral arc (not shown here). The reconstruction works well when there are the stations on both the north and south sides of the aruroral arc (Aso et al., 1998).

Figure 6 exhibits the reconstructed differential flux of the incident electrons at points B and D in Fig. 3a. The reconstruction is quite good for the no-noise case (blue curve), where no noise means that both the mean and standard deviation of noise are zero. Even with the noise (green and red curves), the position of E_P in the reconstruction is almost the same as that for the incident electrons. On the other hand, the deviation of the differential flux increases with increasing image noise and underestimation of the flux can be seen at E_P.

The additional peaks seen in Fig. 6b are attributed to the observational system of auroral luminosity, i.e., the matrices $\mathbf{P}_1$ and $\mathbf{M}_1$. The solution $\hat{\boldsymbol{f}}$ of $\min[\varphi(\boldsymbol{f}; w_j)]$ can be expressed as a linear combination of the singular vectors of a matrix which is a function of $\mathbf{P}_1$ and $\mathbf{M}_1$. When the gray level noise is added, the singular vectors with small singular values are neglected and the contribution of the singular vectors with large singular values to $\hat{\boldsymbol{f}}$ stands out, which results in the appearance of the additional peaks.

Here we briefly describe the errors of the inversion results. The standard deviation of the i-th element of the reconstructed differential flux ($\hat{\boldsymbol{f}}$) can be roughly approximated by $\sqrt{\sigma^2/\left(\varphi''(\hat{\boldsymbol{f}})\right)_{i,i}}$, where σ^2 is the variance of the prior distribution in Eq. (13) and $\left(\varphi''(\hat{\boldsymbol{f}})\right)_{i,i}$ is the second order derivative of $\varphi(\boldsymbol{f})$ with respect to f_i at $\boldsymbol{f} = \hat{\boldsymbol{f}}$. As σ^2 is unknown, it was roughly estimated from $\sigma^2 \approx \left\|\nabla^2 \hat{\boldsymbol{f}}\right\|^2 / n$. The obtained standard deviations were about 10 to 60 percent of the reconstructed differential flux for the cases tested in this paper.

We emphasize that the non-negative constraint of the differential flux plays an important role in the reconstruction. If we do not use CNA data and the non-negative constraint, the inverse problem becomes the linear equations, which can be more easily solved by the CG method. However, the differential flux reconstructed by the CG method without the non-negative constraint often included negative elements.

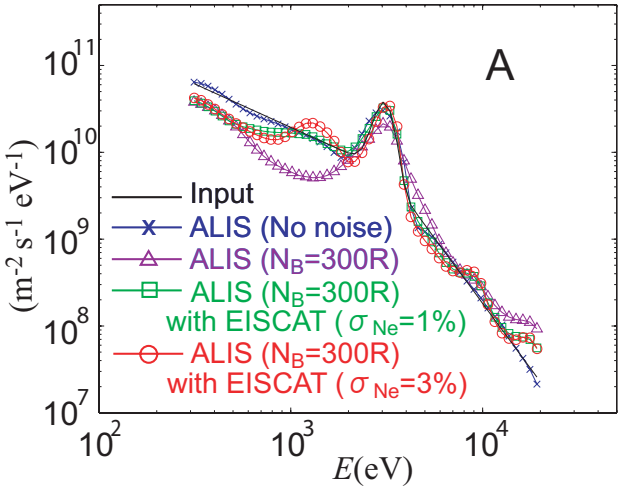

Fig. 7. The differential flux of the incident electrons at point A reconstructed from only auroral images (purple curve) and from both the auroral images and the EISCAT electron density (green and red curves). A background noise of 300 R was added to the image data and a Gaussian noise with a mean of $0\,\mathrm{m}^{-3}$ and a 1% (3%) standard deviation. Black and blue curves correspond to the differential flux of the original incident electrons and the differential flux reconstructed from auroral images with no noise, respectively.

4.2 Reconstruction from auroral images and electron density

Figure 7 shows the reconstructed differential flux at point A, which corresponds to the line-of-sight direction of the EISCAT radar. The purple curve corresponds to a reconstruction from only auroral images with a background noise of 300 R. The green (red) curve corresponds to a reconstruction using both the auroral images and the electron density with added Gaussian noise with a mean of $0\,\mathrm{m}^{-3}$ and a 1% (3%) standard deviation. From this figure, the differential flux reconstructed from only auroral images is less than the incident flux for energies at and below E_P and greater than the incident flux for energies above E_P (purple curve). It is evident that the underestimation and overestimation of the differential flux were significantly corrected by using the electron density from the EISCAT radar. The improvement of the reconstruction is limited to $E > 700$ eV, because the electron density at $z < 170$ km was used for the inversion.

Note that the correction of the differential flux is significant only around A, because the observation region of the EISCAT radar is limited to along the geomagnetic field line at A. In addition, the temporal resolution of the EISCAT radar data is usually lower than that of the ALIS data. Nevertheless, the correction imparted by the radar data is very important, because the next generation EISCAT_3D facility will be capable of measuring the ionosphere in a wide area at high-spatial and high-temporal resolutions. We are planning to apply this method to the 3-D ionospheric electron density observed by the EISCAT_3D in future.

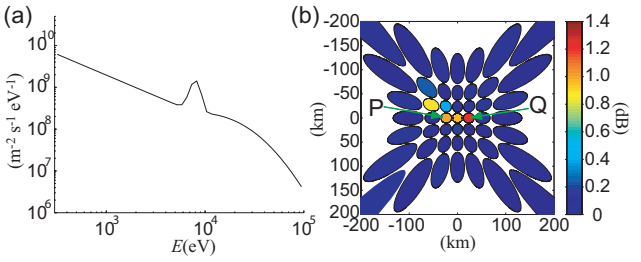

Fig. 8. (a) Energy distribution of the incident electrons at the center of the arc. The distribution is similar to Fig. 3b, but the high-energy tail has been replaced with a kappa distribution. **(b)** CNA detected with the IRIS at Kilpisjärvi. Top and right correspond to the northward and eastward direction, respectively. Note that the center of this panel corresponds to the position of Kilpisjärvi. Each colored area shows −3 dB contour of the main beam. Gaussian noise with a mean of 0 dB and a standard deviation of 0.03 dB has been added to the CNA data. P and Q are the beams where the precipitating electrons at points C and E in Fig. 3a contribute to the generation of CNA.

4.3 Reconstruction from auroral images and CNA

It is well known that CNA is sensitive to precipitating electrons with energies greater than 20×10^3 eV. Thus, the energy range for the calculation was extended to $300 \sim 100 \times 10^3$ eV. Furthermore, a kappa distribution was adopted for the high-energy tail of the incident electrons, instead of the power-law distribution used in Sects. 4.1 and 4.2. The kappa distribution is often observed in diffuse auroras, and is thought to be attributed to the electrons in the plasma sheet. The high-energy tail is given by

$$f(E) \propto E\left(1+\frac{E}{\kappa E_\mathrm{P}}\right)^{-\kappa-1} \quad \text{for} \quad E > E_\mathrm{P}. \tag{20}$$

The energy distribution becomes harder with decreasing κ and it approaches a Maxwellian distribution as κ goes to infinity. It was assumed that the distribution of total energy flux is same as in Fig. 3a and E_P in Eq. (20) is equal to E_P in the Gaussian distribution. E_P and κ were fixed everywhere to 8×10^3 eV and 6, respectively. Figure 8a and b show the energy distribution of the incident electrons at the center of the arc and CNA observed with the IRIS at Kilpisjärvi, including a Gaussian noise distribution with a mean of 0 dB and a standard deviation of 0.03 dB, respectively.

To examine the usefulness of CNA for the inversion, we added a well-characterized noise to image data for four stations located to the south of Skibotn. The background noise decreases gradually from 200 R on the northern edge (closest to the horizon) to 0 R on the southern edge (farthest from the horizon). On the other hand, a uniform background noise of 100 R was added to the image at Skibotn. Such spatial gradient of the noise tends to make the reconstructed energy spectra harder than the input energy spectra.

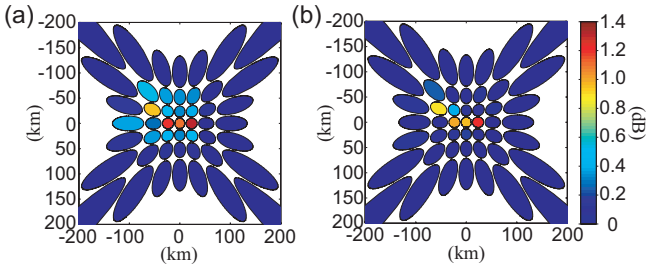

Fig. 9. **(a)** CNA calculated by using the differential flux reconstructed from ALIS images only. **(b)** CNA obtained by using the differential flux reconstructed from both auroral images and CNA.

Figure 9a exhibits CNA obtained by using the differential flux reconstructed from ALIS images only. CNA in this figure is greater than the observed CNA (shown in Fig. 8b) in the auroral precipitation region. Figure 9b shows CNA calculated by using the differential flux retrieved from both auroral images and CNA. It was confirmed by comparing this figure with Fig. 8b that the minimization problem ($\min[\varphi(\boldsymbol{x}; w_1, w_3)]$) including CNA data was properly solved.

Figure 10 shows the differential flux at points C and E (in Fig. 3a) reconstructed from both the auroral images and CNA (red curve), together with the reconstruction from the images only (green curve). The differential flux at points C and E contributed to the generation of CNA for the beams P and Q, respectively (see Fig. 8b). The reconstructed differential flux was slightly corrected by using CNA in the very-high-energy range ($E > 70 \times 10^3$ eV). The energy spectra became smoother by using CNA data, indicating that the relative weight of the smoothness constraint increased in this case. On the other hand, the differential flux was poorly reconstructed in the lower-energy range including the peak at $E = E_{\mathrm{P}}$.

We extended the energy range up to 100×10^3 eV to incorporate CNA data into our method, however, that made it difficult to reconstruct the differential flux in the low-energy range. The low-energy differential flux is prone to be affected by the observational noise, because the 427.8-nm emission and the electron density enhancement caused by the low-energy flux are very small. In addition, the reconstruction error in the high-energy differential flux arisen from the observational noise also affects the emission and the electron density at high altitude, resulting in the error in the low-energy differential flux.

Moreover, the atmospheric parameters such as the neutral density, the neutral temperature, the electron-neutral collision frequency, and the effective recombination coefficient were regarded as the known quantities in this paper. However, these parameters are generally unknown and involve an ambiguity. In particular, there is a large amount of ambiguity in the effective recombination coefficient in the ionospheric

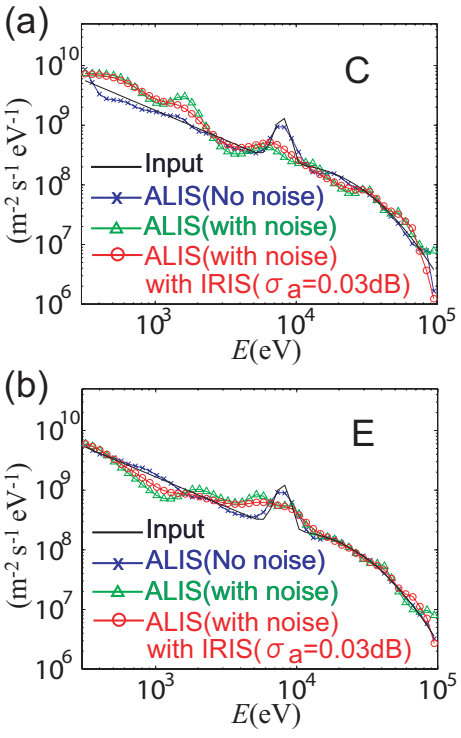

Fig. 10. **(a)** The differential flux of incident electrons at points C and E in Fig. 3a reconstructed from the images only (green curve) and from both the auroral images and CNA (red curve). The format of this figure is similar to that of Fig. 7.

D region (Penmann, 1979), which causes an uncertainty of the reconstructed high-energy differential flux.

Therefore, we conclude that it is difficult at this stage to use CNA data when applying the G-ACT to actual data. Nevertheless, it is worth further investigating how to make use of CNA for the energy reconstruction, as it is the unique data measured from the ground that includes the significant information of the high-energy flux. To extend the energy range, it may be necessary to add the other information of the low-energy electron flux as well as of the high-energy electron flux. For instance, auroral images at different wavelength bands (ex., 844.6 nm) will improve the differential flux in the low-energy range. It may also be effective to make an a priori assumption about the shape of the high energy tail.

5 Conclusions

We provided the concrete algorithm of the Generalized-Auroral Computed Tomography to reconstruct the energy and spatial distribution of a precipitating electron flux from multi-instrument data. Based on a Bayesian model, the inverse problem was formulated as a maximization of the posterior probability. This inversion method enables us to utilize not only auroral images, but also the ionospheric electron density, CNA, and prior information on the incident

Table A1. Simulation parameters.

Parameter	Value	References
I	12.6°	–
$\frac{A_{0-1}q_{0-0}}{\sum_v A_{0-v}}$	0.197	Vallance Jones (1974)
$\Delta\varepsilon$	350 eV	Sergienko and Ivanov (1993)
$\Delta\varepsilon_{\rm ion}$	35.5 eV	Semeter and Kamalabadi (2005)
$\lambda(z,E)$	–	Semeter and Kamalabadi (2005)
$R(E)$	$4.30\times10^{-6}+5.36\times10^{-5}E^{1.67}$ [kg m^{-2}] (E is in keV)	Rees (1989)
$\rho(z)$	calculated from MSIS90 model	Hedin (1991)
$p(z)$	calculated from MSIS90 model	Hedin (1991) Sergienko and Ivanov (1993)
$\alpha(z)$	$4.30\times10^{-12}\exp(-2.42\times10^{-2}z)$ $+8.16\times10^{6}\exp(-0.524z)$ [m^3 s^{-1}] (z is in km)	Gledhill (1986)

electrons. It was confirmed that the differential flux of incident electrons is well reconstructed from the ALIS images for the low-noise cases. We demonstrated in a case study that the combination of the ALIS images with the electron density profile from the EISCAT radar is useful for reconstructing the precipitating flux more accurately. On the other hand, it is difficult at this stage to use CNA data when applying the G-ACT method, as the extension of energy range to about a hundred keV causes difficulty in the reconstruction of the low-energy electron flux.

It should be noted again that the reconstruction test was performed only for a few specific cases in this paper. The test should be performed for various situations of the form and location of aurora, the location of stations, and noise in the observational data, which remains as future work. We expect that this method will become a useful analysis tool for analyzing many kinds of data obtained by the comprehensive observation of auroras. In particular, the 3-D ionospheric parameters measured by the new EISCAT_3D facility will be a most interesting target for this method in the near future.

Appendix A

Derivation of $\mathbf{m_1}$ and $\mathbf{m_2}$

In this section, we describe how to obtain the matrix operators $\mathbf{m}_1$ and $\mathbf{m}_2$ in Sect. 2.2. The energy deposition rate $\varepsilon(z)$ [eV m^{-3} s^{-1}] due to the incident electron flux at an altitude of z is given by

$$\varepsilon(z)=\sec(I)\rho(z)\int\frac{\lambda(s(z)/R(E))Ef(E)}{R(E)}dE, \tag{A1}$$

where I [radian] is the angle between the vertical axis and the magnetic field line, $\rho(z)$ [kg m^{-3}] is the atmospheric mass density, $R(E)$ [kg m^{-2}] is the range of incident electrons with an energy of E, and λ is an energy dissipation function that is dependent on $s(z)/R(E)$. $s(z)$ [kg m^{-2}] is defined as follows:

$$s(z)=\sec(I)\int_z^\infty\rho(z)dz. \tag{A2}$$

The N_2^+ (427.8 nm) emission is due to the transition from $N_2^+(B^2\Sigma_u^+)_{v=0}$ to $N_2^+(X^2\Sigma_g^+)_{v=1}$. According to Sergienko and Ivanov (1993), the volume emission rate $L(z)$ [m^{-3} s^{-1}] is approximated by

$$L(z)=\frac{A_{0-1}q_{0-0}}{\sum_v A_{0-v}}w(z)=\frac{A_{0-1}q_{0-0}}{\sum_v A_{0-v}}\frac{p(z)\varepsilon(z)}{\Delta\varepsilon}, \tag{A3}$$

where A_{0-1} is the Einstein coefficient for the transition from $N_2^+(B^2\Sigma_u^+)_{v=0}$ to $N_2^+(X^2\Sigma_g^+)_{v=1}$, $w(z)$ [m^{-3} s^{-1}] is the production rate of $N_2^+(B^2\Sigma_u^+)$, q_{0-0} is the Franck-Condon factor of the electronic transition from $N_2(X^1\Sigma_g^+)_{v=0}$ to $N_2^+(B^2\Sigma_u^+)_{v=0}$, $p(z)$ is the probability of $\varepsilon(z)$ used to excite N_2, and $\Delta\varepsilon$ [eV] is the excitation energy cost of $N_2^+(B^2\Sigma_u^+)$. The production rate of $N_2^+(B^2\Sigma_u^+)$, $w(z)$, can be obtained by dividing the energy dissipated to excite N_2 (= $p(z)\varepsilon(z)$) by the excitation energy cost of $N_2^+(B^2\Sigma_u^+)$, $\Delta\varepsilon$. Sergienko and Ivanov (1993) demonstrated that $\Delta\varepsilon$ is approximately independent of the energy of the incident electrons.

Similarly to the volume emission rate, the square of electron density, $D(z)$ [m^{-6}], enhanced by the incident electrons at z is given by

$$D(z)=\frac{q_{\rm ion}(z)}{\alpha(z)}=\frac{\varepsilon(z)}{\alpha(z)\Delta\varepsilon_{\rm ion}}, \tag{A4}$$

where $q_{\rm ion}(z)$ [m^{-3} s^{-1}] is the ionization rate due to the incident electrons, $\alpha(z)$ [m^3 s^{-1}] is the effective recombination coefficient, and $\Delta\varepsilon_{\rm ion}$ [eV] is the energy used to produce a pair of ion and electron.

If f_j is $f(E)$ in the range of $E_j \le E \le E_j + \Delta E_j$ and if L_i and D_i are $L(z)$ and $D(z)$ in $z_i \le z \le z_i + \Delta z_i$, L_i and D_i are obtained from Eqs. (A1), (A3), and (A4) as follows;

$$L_i = \sum_j m_{1,ij} f_j, \tag{A5}$$

$$D_i = \sum_j m_{2,ij} f_j, \tag{A6}$$

where $m_{1,ij}$ and $m_{2,ij}$ are the (i, j)-th entries of $\mathbf{m}_1$ and $\mathbf{m}_2$, respectively, which are given by

$$m_{1,ij} = \frac{A_{0-1} q_{0-0}}{\sum_v A_{0-v}} \frac{\sec(I)}{\Delta\varepsilon} \rho(z_i) p_i(z_i) \frac{\lambda\left(z_i, E_j\right) E_j \Delta E_j}{R(E_j)}, \tag{A7}$$

$$m_{2,ij} = \frac{\sec(I)}{\Delta\varepsilon_{\text{ion}}} \frac{\rho(z_i)}{\alpha(z_i)} \frac{\lambda\left(z_i, E_j\right) E_j \Delta E_j}{R(E_j)}. \tag{A8}$$

The parameters used for the calculation is summarized in Table A1.

Acknowledgements. This work was supported by Transdisciplinary Research Integration Center, Research Organization of Information and Systems. This work was also supported by KAKENHI (19740307). The authors thank G. Ueno from the institute of Statistical Mathematics for his valuable comments.

Topical Editor K. Kauristie thanks two anonymous referees for their help in evaluating this paper.

References

Aggarwal, K. M., Nath, N., and Setty, C. S. G. K.: Collision frequency and transport properties of electrons in the ionosphere, Planet. Space Sci., 27, 753—768, 1979.

Aso, T., Hashimoto, T., Abe, M., Ono, T., and Ejiri, M.: On the analysis of aurora stereo observations, J. Geomagn. Geoelectr., 42(5), 579–595, 1990.

Aso, T., Ejiri, M., Miyaoka, H., Ono, T., Hashimoto, T., Yabu, T., and Abe, M.: Aurora stereo observation in Iceland, Proc. NIPR Symp. Upper Atmos. Phys., 6, 1–14, 1993.

Aso, T., Ejiri, M., Urashima, A., Miayoka, H., Steen, Å., Brändström, U., and Gustavsson, B.: First results of auroral tomography from ALIS-Japan multi-station observations in March, 1995, Earth Planets Space, 50, 81–86, 1998.

Aso, T., Gustavsson, B., Tanabe, K., Brändström, U., Sergienko, T., and Sandahl, I.: A proposed Bayean model on the generalized tomographic inversion of aurora using multi-instrument data, Proc. 33rd Annual European Meeting on Atmospheric Studies by Optical Methods, IRF Sci. Rep., 292, 105–109, 2008.

Brändström, U.: The Auroral Large Imaging System – Design, operation and scientific results, IRF Sci. Rep. 279, Kiruna, 184 pp., 2003.

Dashkevich, Zh. V., Ivanov, V. E., and Khudukon, B. Z.: Features of stable diffuse arcs observed by means of auroral tomography, Ann. Geophys., 25, 1131–1139, doi:10.5194/angeo-25-1131-2007, 2007.

Detrick, D. L. and Rosenberg, T. J.: A phased-array radiowave imager for studies of cosmic noise absorption, Radio Sci., 25(4), 325–338, 1990.

Folkestad, K., Hagfors, T., and Westerlund, S.: EISCAT: An updated description of technical characteristics and operational capabilities, Radio Sci., 18(6), 867–879, 1983.

Frey, S. and Frey, H. U.: Auroral emission profiles extracted from three-dimensionally reconstructed arcs, J. Geophys. Res., 101(A10), 21731–21741, 1996.

Gledhill, J. A.: The effective recombination coefficient of electrons in the ionosphere between 50 and 150 km, Radio Sci., 21(3), 399–408, 1986.

Gordon, R., Bender, R., and Herman, G. T.: Algebraic Reconstruction Techniques (ART) for three-dimensional electron microscopy and X-ray photography, J. Theor. Biol., 29, 471–481, 1970.

Gustavsson, B.: Tomographic inversion for ALIS noise and resolution, J. Geophys. Res., 103(A11), 26621–26632, 1998.

Gustavsson, B., Steen, Å., Sergienko, T., and Brändström, B. U. E.: Estimate of auroral electron spectra, the power of ground-based multi-station optical measurements, Phys. Chem. Earth Pt. C., 26(1–3), 189–194, 2001.

Hargreaves, J. K. and Detrick, D. L.: Application of polar cap absorption events to the calibration of riometer systems, Radio Sci., 37, 1035–1045, 2002.

Hedin, A. E.: Extension of the MSIS thermosphere model into the middle and lower atmosphere, J. Geophys. Res., 96(A2), 1159–1172, 1991.

Janhunen, P.: Reconstruction of electron precipitation characteristics from a set of multiwavelength digital all-sky auroral images, J. Geophys. Res., 106(A9), 18505–18516, 2001.

Nygrén, T., Markkanen, M., Lehtinen, M., and Kaila, K.: Application of stochastic inversion in auroral tomography, Ann. Geophys., 14, 1124–1133, doi:10.1007/s00585-996-1124-1, 1996.

Penman, J. M., Hargreaves, J. K., and McIlwain, C. E.: The relation between 10 to 80 keV electron precipitation observed at geosynchronous orbit and auroral radio absorption observed with riometers, Planet. Space Sci., 27, 445–451, 1979.

Rees, M. H.: Physics and chemistry of the upper atmosphere, edited by: Houghton, J. T., Rycroft, M. J., and Dessler, A. J., Cambridge University Press, New York, 1989.

Romick, G. J. and Belon, A. E.: The spatial variation of auroral luminosity – II, Planet. Space Sci., 15, 1695–1716, 1967.

Semeter, J. and Kamalabadi, F.: Determination of primary electron spectra from incoherent scatter radar measurements of the auroral E region, Radio Sci., 40, RS2006, doi:10.1029/2004RS003042, 2005.

Sergienko, T. and Ivanov, V.: A new approach to calculate the excitation of atmospheric gases by auroral electron impact, Ann. Geophys., 11(8), 717–727, 1993.

Stenbaek-Nielsen, H. C. and Hallinan, T. J.: Pulsating auroras: Evidence for non-collisional thermalization of precipitating electrons, J. Geophys. Res., 84(A7), 3257–3271, 1979.

Stone, M.: Cross-validatory choice and assessment of statistical predictions (with discussion), J. Roy. Stat. Soc. B, 36, 111–147, 1974.

Strickland, D. J., Daniell Jr., R. E., Jasperse, J. R., and Basu, B.: Transport-theoretic model for the electron-proton-hydrogen atom aurora, 2. Model results, J. Geophys. Res., 98(A12), 21533–21548, 1993.

Tanabe, K.: Projection method for solving a singular system of linear equations and its applications, Numer. Math., 17, 203–214, 1971.

Vallance Jones, A.: Aurora, D. Reidel Publishing Company, Dortrecht, 1974.

Vallance Jones, A., Gattinger, R. L., Creutzberg, F., Harris, F. R., McNamara, A. G., Yau, A. W., Llewellyn, E. J., Lummerzheim, D., Rees, M. H., McDade, I. C., and Margot, J.: The ARIES auroral modelling campaign: Characterization and modelling of an evening auroral arc observed from a rocket and a ground-based line of meridian scanners, Planet. Space Sci., 39(12), 1677–1705, 1991.